Bulletin of Mathematical Biology (2024) 86:126
https://doi.org/10.1007/s11538-024-01354-5

Society for Mathematical Biology

ORIGINAL ARTICLE

An Approximate Bayesian Computation Approach for Embryonic Astrocyte Migration Model Reduction

Tracy L. Stepien[1]

Received: 23 February 2024 / Accepted: 27 August 2024 / Published online: 13 September 2024

Abstract
During embryonic development of the retina of the eye, astrocytes, a type of glial cell, migrate over the retinal surface and form a dynamic mesh. This mesh then serves as scaffolding for blood vessels to form the retinal vasculature network that supplies oxygen and nutrients to the inner portion of the retina. Astrocyte spreading proceeds in a radially symmetric manner over the retinal surface. Additionally, astrocytes mature from astrocyte precursor cells (APCs) to immature perinatal astrocytes (IPAs) during this embryonic stage. We extend a previously-developed continuum model that describes tension-driven migration and oxygen and growth factor influenced proliferation and differentiation. Comparing numerical simulations to experimental data, we identify model equation components that can be removed via model reduction using approximate Bayesian computation (ABC). Our results verify experimental studies indicating that the choroid oxygen supply plays a negligible role in promoting differentiation of APCs into IPAs and in promoting IPA proliferation, and the hyaloid artery oxygen supply and APC apoptosis play negligible roles in astrocyte spreading and differentiation.

Keywords Cell migration · Embryonic development · Retina · Mathematical modeling · Free boundary problem · Continuum model

1 Introduction

The retinal vasculature is vitally important for supplying oxygen and nutrients to the inner layers of the retina, which contain photoreceptor cells and glial cells that convert light signals to electrical and chemical signals that transmit to the brain, resulting in a visual picture. When angiogenesis, the development of the retinal vasculature, does not proceed correctly, it can lead to eye diseases, such as retinopathy of prematurity and diabetic retinopathy, that cause loss of vision (Hellström et al. 2013; Fung et al. 2022).

✉ Tracy L. Stepien
tstepien@ufl.edu

[1] Department of Mathematics, University of Florida, Gainesville, FL, USA

The development of the retinal vasculature begins around mid-gestation in humans and closer to birth in mice and rats (Stone et al. 1995; Saint-Geniez and D'Amore 2004; Fruttiger 2007). However, before endothelial cells form the blood vessel network, astrocytes, a type of glial cell, spread to form a mesh, creating a spatial template for the endothelial cells. The presence of astrocytes and the retinal vasculature are strictly correlated; in mammals, astrocytes and vasculature are either both present or both absent in the retina (Fruttiger 2007). Hence, gaining insight into the mechanisms of astrocyte migration during embryonic development of the retina to assemble a scaffold for subsequent blood vessel formation is key to understanding retinal angiogenesis in both healthy and disease states.

The first mathematical model of retinal angiogenesis to implement astrocytes was the work of Aubert et al. (2011), with later extensions by McDougall et al. (2012) and Watson et al. (2012). Each of these models used partial differential equations to describe the densities of endothelial cells, astrocytes, and growth factors, including the A chain of platelet-derived growth factor (PDGFA) and vascular endothelial growth factor (VEGF), and were based on data from mice. These models focused on the migration of endothelial cells, with astrocytes playing a supporting role. The timeframe of these models included prenatal and postnatal days to capture both the establishment of the astrocyte mesh and the subsequent spreading of endothelial cells to form the vasculature. In Stepien and Secomb (2022), a partial differential equations model based on rat data was developed to focus solely on astrocyte spreading prenatally before angiogenesis occurs, and it was the first model to additionally consider the differentiation of astrocytes. The model of Stepien and Secomb (2022) forms the basis for this study, where we aim to test model assumptions and deduce a reduced model that contains the essential mechanisms describing astrocyte patterning during retinal development.

To compare between various potential models, we implement model comparison using approximate Bayesian computation (ABC) (Sunnåker et al. 2013; Liepe et al. 2014; Sisson et al. 2019). The ABC rejection method produces probability density distributions of estimated parameters that best fit experimental data in situations where the likelihood is not tractable. It has been used in studying cell migration and other biological problems such as those in genetics, ecology, epidemiology, oncology, and systems biology (Tanaka et al. 2006; Vo et al. 2015; Johnston et al. 2016; Browning et al. 2017; da Costa et al. 2018; Dutta et al. 2018; Kursawe et al. 2018; Stepien et al. 2019; Warne et al. 2019; Browning et al. 2020; Carr et al. 2021; Xiao et al. 2021; Martina Perez et al. 2022; Cunha Jr. et al. 2023; Anderson et al. 2024; Wang et al. 2024). We use the results of the ABC rejection method to inform potential reduced models where different terms are removed and test whether they are more representative of the experimental data. This gives insight into terms that are not required to be included in a biologically representative mathematical model.

Our goal is to determine which mechanisms of astrocyte proliferation, differentiation, and apoptosis are essential to include in a mathematical model of embryonic astrocyte migration in the retina to represent the underlying biology. In this paper, we extend the mathematical model of Stepien and Secomb (2022) to include additional components that may play a role in astrocyte spreading and differentiation such as the

hyaloid artery. Applying ABC, we identify reduced models that may better represent experimental data, and subsequently, identify individual terms that are not necessary.

2 Mathematical Model

We briefly review the continuum mechanical model of astrocyte spreading and differentiation as described in Stepien and Secomb (2022) and introduce modifications of the equations that are used in this study. The mathematical model is based on data from the rat experimental model and is assumed to be driven by gradients in tension within the astrocyte layer. Though the retina has a spherical geometry in vivo, experimental measurements are often taken after the retina has been cut and flattened, and thus, axial symmetry about the optic nerve head is assumed. Additionally, as astrocytes migrate in a radial fashion away from optic nerve head (Fruttiger 2007), we consider a one-dimensional spatial model that assumes radial symmetry (Fig. 1A). All variables are represented as functions of radial position r and time t after embryonic day E15. The time period of the model is from embryonic day E15 to the day of birth, E22/P0.

The model is derived from conservation of mass and balance of momentum in radial coordinates. Letting $c_1(r,t)$ and $c_2(r,t)$ be the density of APCs and IPAs on the retinal surface, respectively, the following governing equations were derived in Stepien and Secomb (2022),

$$\text{APCs:} \quad \frac{\partial c_1}{\partial t} = -\frac{1}{\mu r}\frac{\partial}{\partial r}\left(r c_1 T'(c_{\text{tot}})\frac{\partial c_{\text{tot}}}{\partial r}\right) + g_1, \tag{1a}$$

$$\text{IPAs:} \quad \frac{\partial c_2}{\partial t} = -\frac{1}{\mu r}\frac{\partial}{\partial r}\left(r c_2 T'(c_{\text{tot}})\frac{\partial c_{\text{tot}}}{\partial r}\right) + g_2, \tag{1b}$$

where μ is a viscous constant, $c_{\text{tot}} = c_1 + c_2$ is the total astrocyte density, $T(c_{\text{tot}})$ is the tension function that describes how motion is driven at the edge, and g_1 and g_2 are growth functions that can depend on proliferation, differentiation, and apoptosis.

In Stepien and Secomb (2022), the viscous constant for APCs was set to be twice that of the viscous constant for IPAs to better capture the narrow high density region of APCs at the outer edge of the astrocyte disk. In this study, however, we assume that the viscous constant is the same for both the APCs and IPAs. Although rudimentary exploration of parameter values in Stepien and Secomb (2022) failed to reveal a narrow outer rim of APCs when the viscous constants are equal, the numerical method developed here for the model with equal viscous constants is more robust than the numerical method developed in Stepien and Secomb (2022) because it is stable for a larger range of parameter values, and thus, it is better equipped to perform the parameter analysis in this study.

We assume that the tension T in the cell layer is proportional to the difference between two radii: the radius $\bar{r}$ at which the tension drops to zero and the radius r_{ast} of an astrocyte (including its cell processes), which is assumed to be proportional to

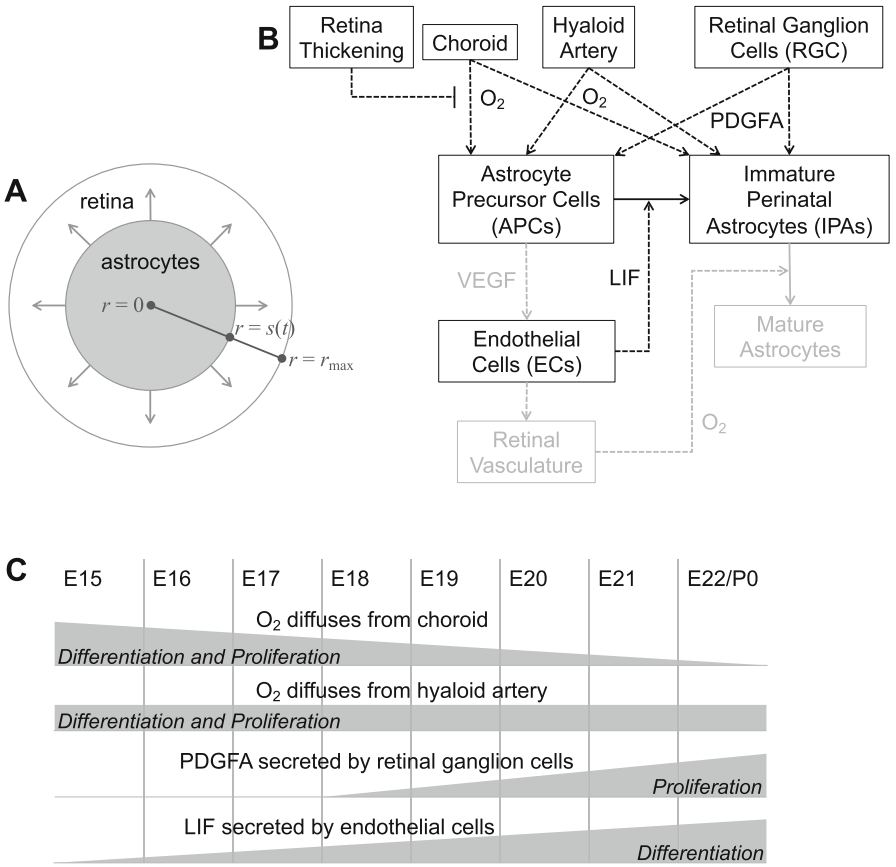

Fig. 1 Schematics of the model configuration and factors influencing astrocyte proliferation and differentiation. **A** Top view of the spreading astrocyte layer, with radial domain $r = [0, r_{\max}]$ and astrocyte moving boundary $r = s(t)$ indicated. **B** Interactions of astrocytes, growth factors, and oxygen. Components in light gray are not explicitly represented in the model. Platelet derived growth factor (PDGFA) produced by retinal ganglion cells (RGCs) and oxygen diffusing from the choroid and hyaloid artery promote proliferation of APCs and IPAs. Leukemia inhibitory factor (LIF) produced by endothelial cells (ECs) and oxygen promote differentiation of APCs into IPAs. **C** Timeline of levels of oxygen and growth factors within the retina. Oxygen diffuses from the choroid and hyaloid artery; the partial pressure levels of choroid oxygen decrease with time as the retina thickens while the levels of hyaloid artery oxygen remain constant. PDGFA is produced by RGCs starting at E18; PDGFA concentration increases with time due to increasing production rate. LIF is produced by ECs starting at E15; LIF concentration increases with time as ECs spread radially

the radius of a disk with area equal to the retinal surface area per cell. This results in

$$T(c_{\text{tot}}) = \kappa\,(r_{\text{ast}} - \bar{r}) = \kappa\left(\frac{1}{\sqrt{\pi\, c_{\text{tot}}}} - \bar{r}\right), \tag{2}$$

where κ is a spring constant (Stepien and Secomb 2022). Parameters with values known or derived from literature are given in Table 1.

Table 1 Model parameters with values that are known or derived from literature

Astrocyte size and tension				
Average cell body radius	$\bar{r}$	7.5×10^{-3}	mm	Stepien and Secomb (2022)
Cell radius including processes	r_{proc}	15.5×10^{-3}	mm	Stepien and Secomb (2022)
Maximum cell density	$c_{\max}$	5300	cells/mm^2	Stepien and Secomb (2022)
Cell density at leading edge	c_e	1000	cells/mm^2	Fruttiger (2007)
Initial cell density at origin	c'_e	$1.021c_e$	cells/mm^2	Stepien and Secomb (2022)
Tension function spring constant	κ	300	mN/mm^2 / Pa	Stepien and Secomb (2022)
Tension at leading edge	T_e	3.10	Pa mm	Stepien and Secomb (2022)
Initial disk radius	s_0	0.17	mm	Chan-Ling et al. (2009)
Oxygen supply				
Oxygen Michaelis constant	P_m	10.5	mmHg	Golub and Pittman (2012)
Choroid oxygen level	P_0	60	mmHg	Secomb (2015)
Diffusivity × solubility of oxygen	$D\alpha$	4.73×10^{-10}	cm^3 O_2/cm/s/mmHg	Secomb (2015)
Oxygen consumption rate	M_0	1.8	cm^3 O_2/100 g/min	Yu et al. (2007); Secomb (2015)
PDGFA and LIF growth factors				
Retina tortuosity	λ	1.6	Dimensionless	Syková and Nicholson (2008)
Retina porosity	ϕ	0.2	Dimensionless	Syková and Nicholson (2008)

Table 1 continued

Maximum PDGFA concentration	q_{maxP}	1	ng/mL	Stepien and Secomb (2022)
Maximum LIF concentration	q_{maxL}	1	ng/mL	Stepien and Secomb (2022)
PDGFA aqueous diffusion constant	D_1	1.32×10^{-6}	cm^2/s	Stepien and Secomb (2022)
LIF aqueous diffusion constant	D_2	1.33×10^{-6}	cm^2/s	Stepien and Secomb (2022)
PDGFA degradation rate	γ_1	4.6	h^{-1}	Stepien and Secomb (2022)
LIF degradation rate	γ_2	4.7	h^{-1}	Stepien and Secomb (2022)
PDGFA production rate	$\bar{\xi}_1$	0.92	ng/(mL h)	Stepien and Secomb (2022)
LIF production rate	$\bar{\xi}_2$	0.94	ng/(mL h)	Stepien and Secomb (2022)
Retinal ganglion cells				
Maximum retinal ganglion cell layer thickness	$L_{\text{RGC,max}}$	46	μm	Braekevelt and Hollenberg (1970)

The terms that comprise the growth functions are the main focus of this study, which are given in terms of proliferation, differentiation, and apoptosis rates by

$$\text{APCs:}\quad g_1(c_1, c_2, P, q_1, q_2) = g_{\text{prolif},1}(c_1, c_2, P, q_1) - g_{\text{diff}}(c_1, P, q_2) - g_{\text{apop},1}(c_1), \tag{3a}$$

$$\text{IPAs:}\quad g_2(c_1, c_2, P, q_1, q_2) = g_{\text{prolif},2}(c_1, c_2, P, q_1) + g_{\text{diff}}(c_1, P, q_2) - g_{\text{apop},2}(c_2), \tag{3b}$$

where P is the partial pressure of oxygen (P_{O_2}) on the retinal surface, and q_1 and q_2 are growth factors to be described below. We retain all the terms that were included in our previous model in Stepien and Secomb (2022), but we add more terms to test additional hypotheses about which mechanisms are essential to include in a mathematical model of embryonic astrocyte migration and differentiation and which are negligible. Figure 1B–C illustrates these potential factors and their levels over time.

For example, our previous model in Stepien and Secomb (2022) assumed that oxygen is supplied only by the choroid vasculature, which is located posterior to the retina and has begun developing during the embryonic development stage that the model is attempting to describe (Berson 1965; Saint-Geniez and D'Amore 2004; Anand-Apte and Hollyfield 2010). We previously neglected the oxygen supply from the hyaloid artery (Shakib et al. 1968; Zhang et al. 1999), whose effect is restricted to a small region around the optic nerve head, but included it in this study as the hyaloid vasculature supplies oxygen and nutrients to the inner part of the eye before the retinal vasculature is formed (Fruttiger 2007). Additionally, Stepien and Secomb (2022) did not include apoptosis terms since cell death is assumed to be negligible during the prenatal period (Chan-Ling et al. 2009). It is included in this study to test if the mathematical model predicts the same hypothesis.

Proliferation is assumed to occur at a rate that depends on the levels of the A chain of platelet-derived growth factor (PDGFA), q_1, oxygen from the choroid, X_c, and oxygen from the hyaloid artery, X_h, in a logistic form to represent the limitation of cell proliferation by crowding on the retinal surface,

$$g_{\text{prolif},i}(c_1, c_2, P, q_1) = \left(\alpha_{i0} + \alpha_{i1}\frac{q_1}{q_{\text{maxP}}} + \alpha_{i2}X_c(r, P) + \alpha_{i3}X_h(r)\right)c_i\left(1 - \frac{c_1 + c_2}{c_{\max}}\right), \qquad i = 1, 2. \tag{4}$$

The values of the proliferation rates α are to be estimated (Table 2).

Differentiation occurs at a rate that depends on the levels of leukemia inhibitory factor (LIF), q_2, oxygen from the choroid, X_c, and oxygen from the hyaloid artery, X_h, in proportion to the amount of APCs present. A mass action term is also included, resulting in

$$g_{\text{diff}}(c_1, P, q_2) = \left(\beta_0 + \beta_1\frac{q_2}{q_{\text{maxL}}} + \beta_2 X_c(r, P) + \beta_3 X_h(r) + \frac{\beta_4}{c_{\max}}c_2\right)c_1. \tag{5}$$

Table 2 Model parameters with values that are to be estimated

Migration constant		
Astrocyte migration constant	μ	force/area $\times$ (length/time)$^{-1}$ = Pa h/mm
Hyaloid artery		
Hyaloid partial pressure of oxygen	P_{hy}	Dimensionless
Radius of hyaloid oxygen extent	r_{hy}	Length = mm
Proliferation rates		
Basal APC rate	α_{10}	1/time = h^{-1}
APC rate with respect to PDGFA	α_{11}	1/time = h^{-1}
APC rate with respect to choroid oxygen	α_{12}	1/time = h^{-1}
APC rate with respect to hyaloid artery oxygen	α_{13}	1/time = h^{-1}
Basal IPA rate	α_{20}	1/time = h^{-1}
IPA rate with respect to PDGFA	α_{21}	1/time = h^{-1}
IPA rate with respect to choroid oxygen	α_{22}	1/time = h^{-1}
IPA rate with respect to hyaloid artery oxygen	α_{23}	1/time = h^{-1}
Differentiation rates		
Basal rate	β_0	1/time = h^{-1}
Rate with respect to LIF	β_1	1/time = h^{-1}
Rate with respect to choroid oxygen	β_2	1/time = h^{-1}
Rate with respect to hyaloid artery oxygen	β_3	1/time = h^{-1}
Mass action rate	β_4	1/time = h^{-1}
Apoptosis rates		
APC rate	η_1	1/time = h^{-1}
IPA rate	η_2	1/time = h^{-1}

The values of the differentiation rates β are to be estimated (Table 2).

Apoptosis occurs at a rate proportional to the amount of APCs or IPAs present,

$$g_{\text{apop},i}(c_i) = \eta_i c_i, \qquad i = 1, 2. \tag{6}$$

The values of the apoptosis rates η are to be estimated (Table 2).

The forms of the oxygen functions X_c and X_h are described in Sect. 2.2, and the growth factors q_1 and q_2 are described in Sect. 2.3, after first stating the boundary and initial conditions in Sect. 2.1.

2.1 Boundary and Initial Conditions

The domain of the astrocytes is considered to be $r \in [0, s(t)]$, where $s(t)$ denotes the dynamic location of the outer edge of the astrocyte layer that forms a moving boundary. The initial location of the edge is $s(0) = s_0$, with value as given in Table 1. Since we assume radial symmetry, we impose a no flux boundary condition at the origin for the APC and IPA cell densities.

On the moving boundary, $s(t)$, we assume that there is a fixed radial tension, T_e, at the cell layer edge, following experimental evidence that traction forces are mainly generated at the leading edge of migrating embryonic astrocytes (De Pascalis et al. 2018). Thus, for a given T_e, the corresponding total cell density at $r = s(t)$ is calculated by inverting (2). We give the parameter values for T_e and c_e in Table 1.

From Stepien and Secomb (2022), the equation describing the velocity at the moving edge of astrocytes, i.e., the Stefan condition, is given by

$$s'(t) = \frac{T'(c_e)}{\mu_1} \frac{\partial c_{\text{tot}}}{\partial r}\bigg|_{r=s(t)}. \tag{7}$$

At $t = 0$, the initial conditions for the APCs and IPAs are assumed to be

$$c_1 = c_e + (c_e' - c_e)\left(1 - \left(\frac{r}{s_0}\right)^2\right), \qquad 0 \le r \le s_0, \tag{8}$$

and $c_1 = 0$ elsewhere, and $c_2 = 0$ everywhere. c_e' is a constant chosen to given an appropriate initial rate of spreading, with value given in Table 1.

2.2 Oxygen Supply

Cell proliferation is dependent on oxygen availability for most cell types (Hubbi and Semenza 2015) and oxygen availability has been identified as a driver of astrocyte differentiation (Zhang et al. 1999; West et al. 2005; Duan et al. 2017). As in Stepien and Secomb (2022), we assume that the contribution of oxygen from the choroid is governed by Michaelis–Menten kinetics,

$$X_c(r, P) = \frac{P}{P_m + P}, \tag{9}$$

where P is the partial pressure of oxygen (P_{O_2}) from the choroid on the retinal surface. The variable P_m is the P_{O_2} at half-maximal consumption with value given in Table 1.

To determine an expression for P, we assume that oxygen diffusion from the choroid is represented by a one-dimensional oxygen consumption model from Popel (1989) that assumes zero-order kinetics,

$$D\alpha \frac{\partial^2 P}{\partial z^2} = M_0, \tag{10a}$$

$$P = P_0, \qquad \text{at } z = 0, \tag{10b}$$

$$\frac{\partial P}{\partial z} = 0, \qquad \text{at } z = L, \tag{10c}$$

where D is the diffusivity and α is the solubility of oxygen in tissue, M_0 is the oxygen consumption rate, P_0 is partial pressure of oxygen in the choroid with values given in Table 1. We previously assumed that there is Michaelis–Menten dependence

of consumption on the retinal surface in Stepien and Secomb (2022), but use the simplified model (10) here to significantly reduce the computational time necessary in our parameter analysis. $L = L(r, t)$ is the thickness of retina (in μm), which was fit to experimental data via regression in Stepien and Secomb (2022) and determined to be

$$L(r,t) = L_{\text{ONH}}(t) - \left(L_{\text{ONH}}(t) - L_{\text{periph}}(t)\right)\left(\frac{r}{r_{\text{ret}}(t)}\right)^2, \qquad r \le r_{\text{ret}}(t), \quad (11)$$

and zero otherwise, where

$$L_{\text{ONH}}(t) = 14.33t + 98.78, \quad (12a)$$
$$L_{\text{periph}}(t) = 13.77t + 72.8, \quad (12b)$$
$$r_{\text{ret}}(t) = 414.7t + 1029.2. \quad (12c)$$

We assume that the form of the hyaloid artery contribution is a Hill-type function that is maximal at the optic nerve head ($r = 0$),

$$X_h(r) = P_{\text{hy}}\left(1 - \frac{r^2}{r_{\text{hy}}^2 + r^2}\right), \quad (13)$$

where P_{hy} and r_{hy} are parameters describing the hyaloid partial pressure of oxygen and radius of hyaloid oxygen extent, respectively, with values to be estimated (Table 2).

2.3 PDGFA and LIF Growth Factors

Various growth factors have been identified that play a role in the proliferation and differentiation of APCs and IPAs. In particular, the A chain of platelet-derived growth factor (PDGFA), which is produced by retinal ganglion cells (RGCs), promotes proliferation (Mudhar et al. 1993; West et al. 2005; Fruttiger 2007; Tao and Zhang 2014) and leukemia-inhibitory factor (LIF), which is produced by endothelial cells, promotes differentiation (Mi and Barres 1999; Mi et al. 2001; Fukushima et al. 2009; Tao and Zhang 2014).

Based on the model in Goriely et al. (2002), we assume that concentrations (in ng/mL) of PDGFA, q_1 and LIF, q_2, satisfy the reaction–diffusion equations

$$\frac{\partial q_i}{\partial t} = \frac{D_i}{\lambda^2 r}\frac{\partial}{\partial r}\left(r\frac{\partial q_i}{\partial r}\right) + \frac{\xi_i(r,t)}{\phi} - \gamma_i q_i, \qquad i = 1, 2, \quad (14)$$

where λ and ϕ are the tortuosity and porosity of the retina, respectively, D_1 and D_2 are the diffusivities of PDGFA and LIF in water, and γ_1 and γ_2 are the degradation rates of PDGFA and LIF. See Table 1 for the values of these parameters. $\xi_1(r, t)$ and $\xi_2(r, t)$ represent the amounts of PDGFA and LIF released into the interstitial space per unit tissue volume per unit time. Based on experimental data, in Stepien and

Secomb (2022) these functions were determined to be

$$\xi_1(r,t) = \bar{\xi}_1 \frac{L_{\mathrm{RGC}}(r,t)}{L_{\mathrm{RGC,max}}} \frac{(t-3)}{4}, \qquad r \le r_{\mathrm{ret}}(t), \quad t \ge 3, \tag{15a}$$

$$\xi_2(r,t) = \bar{\xi}_2, \qquad r \le r_{\mathrm{endo}}(t) = 185t, \tag{15b}$$

and zero otherwise, where the thickness of the RGC layer was fit to experimental data via regression in Stepien and Secomb (2022) and determined to be

$$L_{\mathrm{RGC}}(r,t) = GC_{\mathrm{ONH}}(t) - \left(GC_{\mathrm{ONH}}(t) - GC_{\mathrm{periph}}(t)\right)\left(\frac{r}{r_{\mathrm{ret}}}\right)^2, \qquad r \le r_{\mathrm{ret}}(t), \tag{16}$$

and zero otherwise, where

$$GC_{\mathrm{ONH}}(t) = \max\left\{-3.79t^2 + 31.02t - 23.16\ ,\ 0\right\}, \tag{17a}$$

$$GC_{\mathrm{periph}}(t) = \max\left\{-2.49t^2 + 23.81t - 24.12\ ,\ 0\right\}. \tag{17b}$$

The values of the maximum retinal ganglion cell layer thickness, $L_{\mathrm{RGC,max}}$, and the production rates of PDGFA, $\bar{\xi}_1$, and LIF, $\bar{\xi}_2$, are given in Table 1.

It is assumed that PDGFA and LIF can diffuse outside of the growing astrocyte layer, but that they are unlikely to diffuse far outside of the retina. We consider (14)–(17) on a fixed domain $r \in [0, r_{\max}]$, where we set $r_{\max}$ to be significantly larger than the radius of the retina during the time period that is being simulated. The boundary condition $q_1 = q_2 = 0$ is imposed at $r = r_{\max} = 5$ mm and a no flux condition is imposed at the origin.

2.4 Simulations and Experimental Data

A front-tracking method based on the method of Marshall (1986) was developed to numerically solve the model equations and boundary and initial conditions as described in the previous section. Please see Online Resource 1 Section A for details.

Sample simulations of each model considered in Sect. 4 are illustrated in Fig. 2. These simulations represent best fits for each model. Taking the parameter sets that resulted in the five smallest errors (Sect. 3.1) found using approximate Bayesian computation (Sect. 3), we performed gradient descent using `fminsearch` in MATLAB. The parameter set that resulted in the smallest error after using gradient descent are used in the simulations shown.

The experimental data used for model fitting is illustrated in Fig. 2G in Chan-Ling et al. (2009). It shows 2D stereological maps with the location of astrocyte precursor cells (APCs) and immature perinatal astrocytes (IPAs) in rat retina whole mounts at various embryonic ages. The radius of each cell type over time was determined by measuring the average diameter shown in the maps, and the results are reported in Table 3. Due to the nature of obtaining whole mounts, each time point comes from

different rats, and thus variation from the values reported in Table 3 would be expected in individual rats. However, the data as a whole indicates that the geometry of the APC population is that of an expanding annulus while the IPA population is an expanding disk.

In all the models, the spatial distribution of the APCs and IPAs qualitatively matches experimental data as shown in Fig. 2: the geometry of the APC population is that of an expanding annulus while the IPA population is an expanding disk. However, there is a larger difference in APC versus IPA cell density at the leading edge for Fig. 2C–E than for Fig. 2A–B, indicating that the No APC Apoptosis (Sect. 4.3), No Uniform (Sect. 4.4), and No Bio (Sect. 4.5) models fit the density patterning better than the Full (Sect. 4.1) and No Hyaloid (Sect. 4.2) models. Additionally, the moving boundary location fits the experimental data well for all models, with the Full model fitting the best.

3 Parameter and Model Comparison Analysis Using Approximate Bayesian Computation (ABC)

We aim to verify which aspects of the mathematical model developed in Sect. 2 are essential to explain the patterning of APCs and IPAs during embryonic development of the retina. We use the approximate Bayesian computation (ABC) rejection method (Sunnåker et al. 2013; Liepe et al. 2014; Sisson et al. 2019) to determine representative probability distributions of the parameters and inform potential model reductions. We additionally will then compare between these various models.

We implement the ABC rejection method in the following steps:

(1) *Prior distribution* Use Latin hypercube (LH) sampling to generate a near-random sample of sets of parameter values from a multi-dimensional distribution, which allows for sampling the multi-dimensional model parameter space efficiently (Sisson et al. 2019; Burkardt 2021). In particular, if there are n parameters to be estimated from Table 2, there is an n-dimensional space of LH points. The set of all the ith elements of the LH points forms a prior distribution for the ith parameter.

Upper and lower bounds of the parameter ranges are chosen based on a combination of order of magnitude estimates of biologically relevant values and numerical simulation outputs. For example, an upper bound for μ can be determined by setting an upper bound for the initial time step (see equation (A2.a) in Online Resource 1 Section A). Simulations with parameter values that were too large resulted in numerical errors.

(2) *Posterior distribution* Run a simulation for each parameter set and calculate the error by comparing the simulation to experimental data (Sect. 3.1). If the error is smaller than a specified threshold value τ, it is sufficiently close to the experimental data and the parameter set is accepted. If the error is larger than the threshold τ, the parameter set is rejected. The set of all the ith elements of the accepted parameter sets forms a posterior distribution for the ith parameter.

We fit numerous probability distributions (Normal, Lognormal, Gamma, Exponential, Weibull, and Uniform) to each of the posterior distributions and then determine the best fitting probability distribution by minimizing the 1-Wasserstein metric (earth

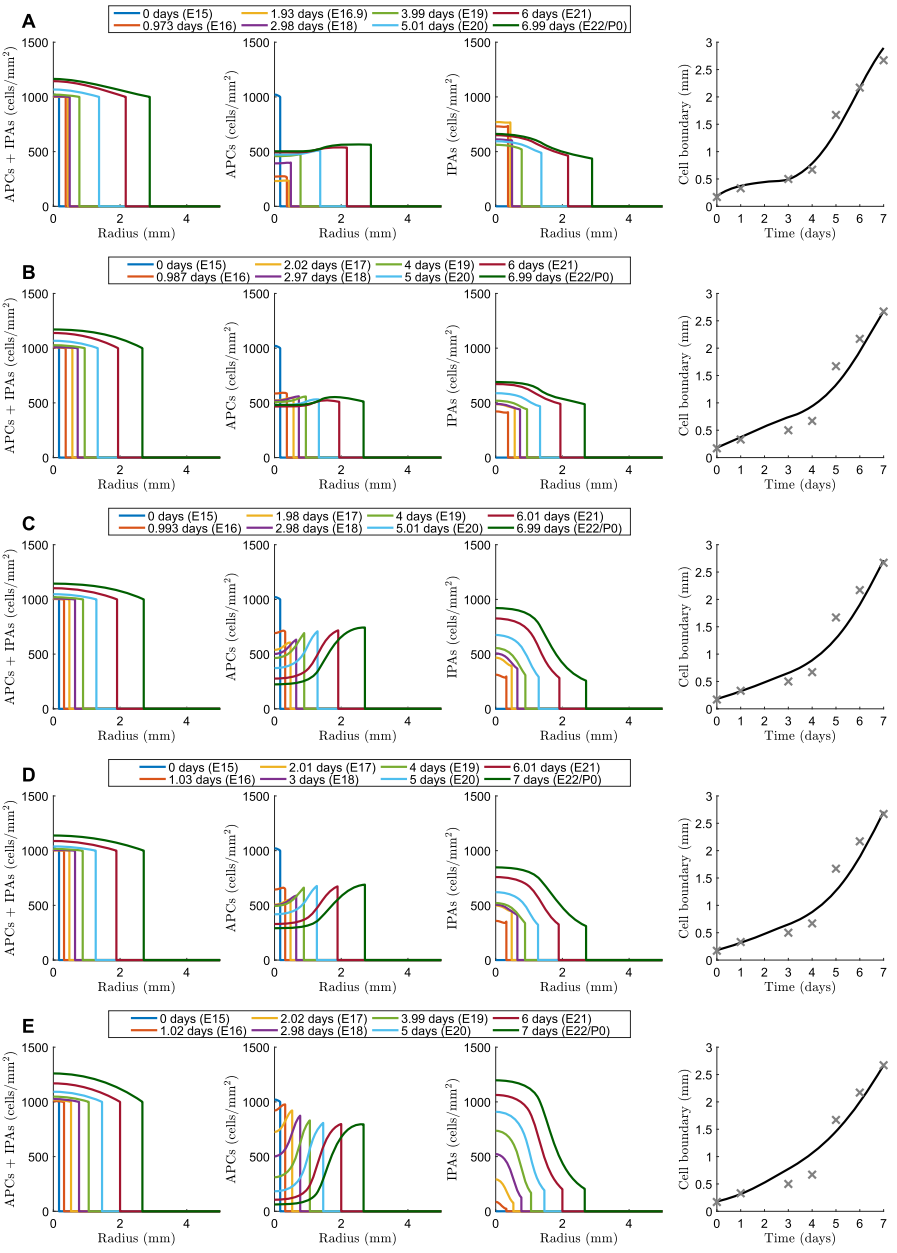

Fig. 2 Cell densities of astrocyte precursor cells (APCs) and immature perinatal astrocytes (IPAs) and the location of the moving boundary of astrocytes (×: observed astrocyte spread from experimental data). Parameter values are listed in Online Resource 1 Section B. **A** Full model (Sect. 4.1); $\mathcal{E} = 2.5207$. **B** No Hyaloid model (Sect. 4.2); $\mathcal{E} = 2.9913$. **C** No APC Apoptosis model (Sect. 4.3); $\mathcal{E} = 2.8072$. **D** No Uniform model (Sect. 4.4); $\mathcal{E} = 2.8046$. **E** No Bio model (Sect. 4.5); $\mathcal{E} = 2.8495$.

Table 3 Radius in mm of astrocyte precursor cells (APCs) and immature perinatal astrocytes (IPAs) as measured from Fig. 2G in Chan-Ling et al. (2009)

	E15	E16	E18	E19	E20	E21	E22/P0
APCs	0.17	0.33	0.5	0.67	1.67	2.17	2.67
IPAs	0	0.04	0.08	0.33	1	1.5	2

mover's distance). This allows for a quantitative characterization of the posterior distributions and an additional assessment for skewness.

To deduce which mathematical model best fits the experimental data, one can compare the marginal probabilities $p(\text{model} \mid \text{data})$ among various models. The ABC rejection model selection algorithm in the joint space-based approach is to: (1) choose a model uniformly randomly from a set of model indicators $\{m_1, m_2, \ldots, m_k\}$, (2) sample parameters for that model from the prior distributions, (3) run a simulation for the parameter set and calculate the error, (4) accept the model and parameter set if the error is less than τ (Grelaud et al. 2009; Toni and Stumpf 2009). In this set up, we do not use Latin hypercube sampling but instead sample the parameters from a uniform prior distribution with the same lower and upper bounds.

The marginal posterior distribution is approximated by

$$p(m_i \mid \text{data}) \approx \frac{\text{Number of accepted parameter sets for model } m_i}{\text{total Number of accepted parameter sets}}. \tag{18}$$

Then to compare models m_i and m_j, compute their posterior ratio

$$\frac{p(m_i \mid \text{data})}{p(m_j \mid \text{data})} = \frac{p(\text{data} \mid m_i)}{p(\text{data} \mid m_j)} \frac{p(m_i)}{p(m_j)} = B_{ij} \frac{p(m_i)}{p(m_j)}, \tag{19}$$

where B_{ij} is the Bayes factor. Assuming that the model priors are equal, $p(m_i) = p(m_j)$, then the posterior ratio equals the Bayes factor (Grelaud et al. 2009; Toni and Stumpf 2009; Francois and Laval 2011; Sunnåker et al. 2013). When the Bayes factor is close to 1, the evidence against m_j (and in favor of m_i) is very weak, and as the Bayes factor increases, the evidence strengthens (Kass and Raftery 1995).

3.1 Error Function

The total error we define to compare between simulations and experimental data, $\mathcal{E}$, consists of the sum of the errors due to three different aspects: time ($\mathcal{E}_{\text{time}}$), radius ($\mathcal{E}_{\text{radius}}$), and density ($\mathcal{E}_{\text{density}}$).

The time error, $\mathcal{E}_{\text{time}}$, penalizes the numerically calculated moving boundary of the astrocytes either slowing down and stalling before the 7 simulated days between E15–E22/P0 has elapsed or speeding up and advancing too far into the retina. We set this numerically simulated time error to be the absolute error

$$\mathcal{E}_{\text{time}} = \left|7 - (\text{last simulated time point})\right|. \tag{20}$$

The radius error, $\mathcal{E}_{\text{radius}}$, compares the distance that the astrocytes have spread over time between the simulations, from the location of the moving boundary $s(t)$, and experimental data, from the radius of APCs as listed in Table 3 (Sect. 2.4). We note that the data was collected on days E15–E16 and E18–E22/P0, so there is no data for day E17. Additionally, since we specify that the initial disk radius s_0 (Table 1) in the numerical simulations is the same as the APC radius on day E15 (Table 3), there are hence only 6 data points at which to measure differences. We set the radius error to be the L^1-norm

$$\mathcal{E}_{\text{radius}} = \sum_{t \in T} \big| (\text{actual radius}) - (\text{simulated radius}) \big|, \tag{21}$$

where the set $T = \{\text{E16}, \text{E18}, \text{E19}, \text{E20}, \text{E21}, \text{E22/P0}\}$.

The density error, $\mathcal{E}_{\text{density}}$, compares the density patterning of APCs versus IPAs. The stereological maps from Fig. 2G in Chan-Ling et al. (2009) (Sect. 2.4) indicate where APC density is higher versus where IPA density is higher. In particular, at radii less than the IPA radius listed in Table 3, the density of IPAs is larger than the APC density. At radii between the IPA radius and the APC radius listed in Table 3, the density of APCs is larger than the IPA density. The density error is based on the Jaccard distance, which is a measure of the distance between two sets, and is given by

$$\mathcal{E}_{\text{density}} = \frac{1}{6} \sum_{t \in T} \left[\left(1 - \frac{|A_t^{\text{APC}} \cap B_t^{\text{APC}}|}{|A_t^{\text{APC}} \cup B_t^{\text{APC}}|} \right) + \left(1 - \frac{|A_t^{\text{IPA}} \cap B_t^{\text{IPA}}|}{|A_t^{\text{IPA}} \cup B_t^{\text{IPA}}|} \right) \right], \tag{22}$$

where A_t is the set of spatial grid nodes in the simulation at time t (see Online Resource 1 Section A for details on the finite difference numerical method) and B_t is the set of spatial grid nodes corresponding to the experimental data, respectively. The superscript "APC" denotes the set of grid nodes at which the APC density is larger than (or equal to) the IPA density, and "IPA" denotes the opposite.

Summing the three errors (20)–(22) together and weighting $\mathcal{E}_{\text{radius}}$ twice as much to assign a higher penalty for a mismatch of the moving boundary location, we obtain the total error,

$$\mathcal{E} = \mathcal{E}_{\text{time}} + 2\mathcal{E}_{\text{radius}} + \mathcal{E}_{\text{density}}. \tag{23}$$

There are cases where we set the total error to a large number (in particular, $\mathcal{E} = 10^4$) to signify a very poor fit: (1) if the last simulated time point is strictly greater than 8, (2) if there is a numerical error and the last simulated time point is an imaginary number, (3) if the APC or IPA cell density, c_1 or c_2, is negative at any spatial node at any time, or (4) if the APC or IPA cell density, c_1 or c_2, is zero at every spatial node at the last simulated time point.

4 Results

As given in Table 2, there are 18 parameters to be estimated. We begin our analysis by generating 500,000 LH points for the ABC rejection method for the full model (Sect. 4.1). We impose the early stopping criteria requiring error value $\mathcal{E} < 10^4$ so that unrealistic model outcomes are immediately removed (Prangle 2016). The threshold value τ for each model was chosen such that approximately 1% of the remaining parameter sets in the prior distribution are accepted (see Online Resource 1 Section C). We subsequently identify parameter values to set equal to zero by looking for right-skewed posterior distributions, and analyze various nested reduced models (Sects. 4.2–4.5).

4.1 Full Model (18 Parameters)

The posterior distributions obtained using the full model with all 18 parameters and threshold value $\tau = 7.25$ are illustrated in Fig. 3. We observe from Fig. 3 that the posterior distributions best fit three different types of classic distributions: Uniform U(lower, upper), Normal $N(\mu, \sigma)$, and Weibull $W(A, B)$, and the corresponding distribution parameters are given in Table 4.

To identify candidates for parameters that may not be essential to include in the mathematical model, we look for parameters with histograms that have a heavy density near zero and corresponding best fitting probability distribution that is right-skewed. We set these parameters equal to zero in a reduced model in the next section.

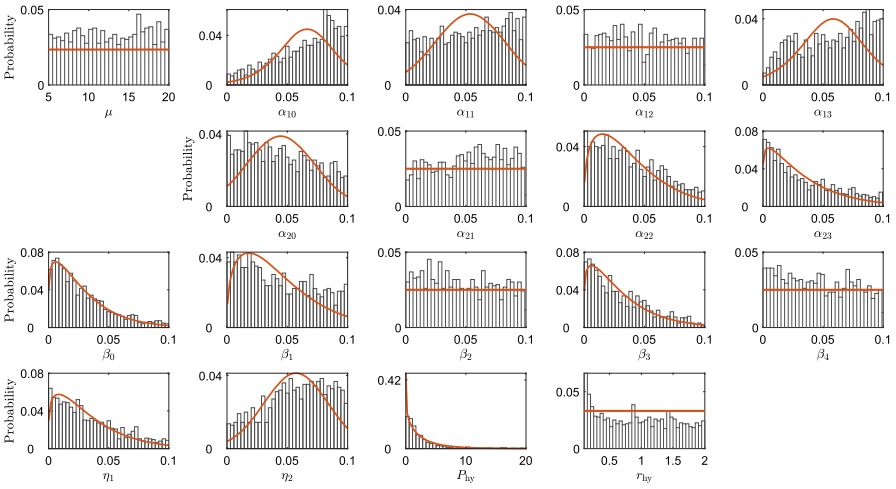

Fig. 3 ABC posterior distributions of all 18 parameters to be estimated (Table 2) for the full model (Sect. 4.1) obtained from using Latin hypercube (LH) sampling with 500,000 LH points as prior distributions as described in Sect. 3. The parameter sets with error (23) less than threshold $\tau = 7.25$ are shown in the histograms. The solid red curves represent the best fitting probability distribution via minimizing the 1-Wasserstein metric (Table 4)

Table 4 Best fitting probability distributions for each parameter in each model via minimizing the 1-Wasserstein metric (earth mover's distance)

Model	Full	No Hyaloid	No APC Apoptosis	No Uniform	No Bio
Number of parameters	18	13	11	9	9
Section	4.1	4.2	4.3	4.4	4.5
μ	$U(5, 20)$	$U(5, 20)$	$W(14.6639, 3.4980)$	$W(14.9277, 3.6459)$	$W(15.0077, 3.7096)$
α_{10}	$N(0.0642, 0.0258)$	$W(0.0815, 4.6919)$	$N(0.0351, 0.0177)$	$N(0.0430, 0.0162)$	$N(0.0308, 0.0128)$
α_{11}	$N(0.0536, 0.0289)$	$U(0, 0.1)$	$U(0, 0.1)$	–	$N(0.0453, 0.0277)$
α_{12}	$U(0, 0.1)$	$U(0, 0.1)$	$N(0.0428, 0.0264)$	$W(0.0415, 1.4811)$	$N(0.0378, 0.0229)$
α_{13}	$N(0.0573, 0.0282)$	–	–	–	–
α_{20}	$N(0.0444, 0.0280)$	$N(0.0536, 0.0264)$	$N(0.0573, 0.0253)$	$N(0.0561, 0.0272)$	$N(0.0585, 0.0254)$
α_{21}	$U(0, 0.1)$	$U(0, 0.1)$	$N(0.0549, 0.0279)$	$N(0.0548, 0.0281)$	$U(0, 0.1)$
α_{22}	$W(0.0413, 1.3477)$	$W(0.0497, 1.5209)$	$W(0.0420, 1.3788)$	$W(0.0371, 1.2499)$	–
α_{23}	$W(0.0351, 1.1089)$	–	–	–	–
β_0	$W(0.0298, 1.1742)$	$W(0.0212, 1.2012)$	–	–	–
β_1	$W(0.0469, 1.3676)$	$N(0.0424, 0.0293)$	$N(0.0449, 0.0275)$	$W(0.0500, 1.6709)$	$\Gamma(2.6819, 0.0165)$
β_2	$U(0, 0.1)$	$W(0.0448, 1.3900)$	$W(0.0451, 1.3607)$	$W(0.0401, 1.3476)$	–
β_3	$W(0.0317, 1.1647)$	–	–	–	–
β_4	$U(0, 0.1)$	$U(0, 0.1)$	$U(0, 0.1)$	–	$U(0, 0.1)$
η_1	$W(0.0356, 1.2076)$	$\Gamma(1.2819, 0.0165)$	–	–	–
η_2	$N(0.0572, 0.0264)$	$N(0.0413, 0.0250)$	$N(0.0387, 0.0230)$	$N(0.0422, 0.0243)$	$N(0.0359, 0.0217)$
P_{hy}	$W(2.7216, 0.08756)$	–	–	–	–
r_{hy}	$U(0.1, 2)$	–	–	–	–

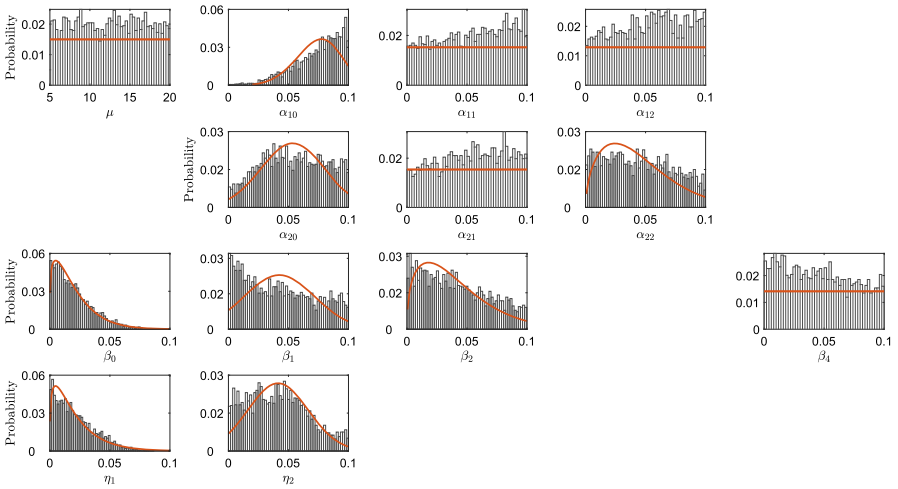

Fig. 4 ABC posterior distributions of 13 parameters to be estimated (Table 2) for the model (Sect. 4.2) without the hyaloid artery ($\alpha_{13}, \alpha_{23}, \beta_3, P_{\text{hy}}$, and r_{hy} removed) obtained from using Latin hypercube (LH) sampling with 500,000 LH points as prior distributions as described in Sect. 3. The parameter sets with error (23) less than threshold $\tau = 5.25$ are shown in the histograms. The solid red curves represent the best fitting probability distribution via minimizing the 1-Wasserstein metric (Table 4) (Color figure online)

The hyaloid artery parameter P_{hy} is a candidate to set equal to zero since the histogram and the best fitting distribution is a highly right-skewed Weibull distribution on the domain (Fig. 3/Table 4). Though some other parameters have left-skewed distributions and the results may not capture their full posterior distribution, such as α_{10}, α_{11}, α_{13}, and η_2, enlarging the domain of all parameters and re-running the ABC rejection routine still resulted in a highly right-skewed distribution for P_{hy}. Since setting $P_{\text{hy}} = 0$ essentially implies that $X_h(r) = 0$ (13), due to the presence of $X_h(r)$ in Eqs. (4), (5), and (13), this additionally means that terms with the hyaloid artery parameters $\alpha_{13}, \alpha_{23}, \beta_3$, and r_{hy} should also be set equal to zero in the model equations. This results in a nested reduced model with 13 parameters that does not contain the hyaloid artery.

4.2 Model Without the Hyaloid Artery (13 Parameters)

The posterior distributions obtained using the model with 13 parameters without the hyaloid artery ($\alpha_{13}, \alpha_{23}, \beta_3, P_{\text{hy}}$, and r_{hy} removed) with threshold value $\tau = 5.25$ are illustrated in Fig. 4.

We observe from Fig. 4 that the posterior distributions best fit four different types of classic distributions: Uniform U(lower, upper), Normal $N(\mu, \sigma)$, Gamma $\Gamma(a, b)$, and Weibull $W(A, B)$, and the corresponding distribution parameters are given in Table 4. Aiming to reduce the model further, by examining the parameters with histograms that have a heavy density near zero, we set the basal differentiation rate, β_0, and the APC apoptosis rate, η_1, equal to zero in the following section as they are best fit by right-skewed Weibull and Gamma distributions, respectively.

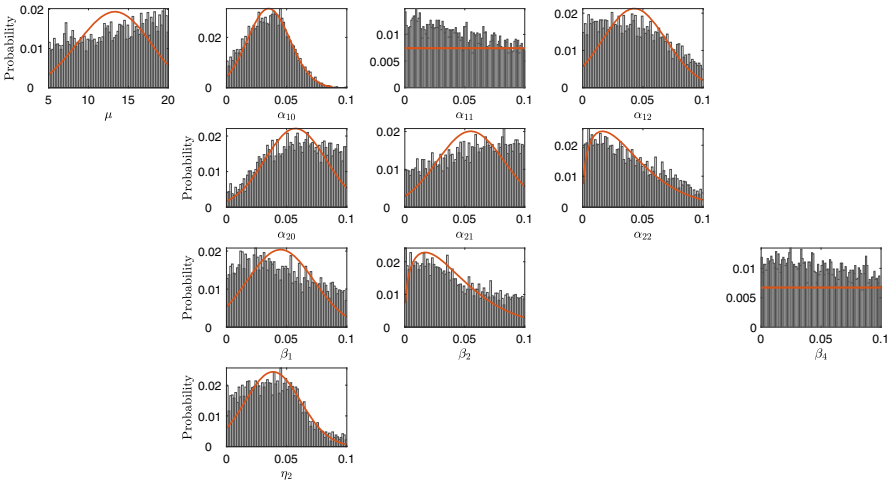

Fig. 5 ABC posterior distributions of 11 parameters to be estimated (Table 2) for the model (Sect. 4.3) without the hyaloid artery, basal differentiation, or APC apoptosis (α_{13}, α_{23}, β_3, P_{hy}, r_{hy}, β_0, and η_1 removed) obtained from using Latin hypercube (LH) sampling with 500,000 LH points as prior distributions as described in Sect. 3. The parameter sets with error (23) less than threshold $\tau = 4.05$ are shown in the histograms. The solid red curves represent the best fitting probability distribution via minimizing the 1-Wasserstein metric (Table 4) (Color figure online)

4.3 Model Without the Hyaloid Artery, Basal Differentiation, and APC Apoptosis (11 Parameters)

The posterior distributions obtained using the model with 11 parameters without the hyaloid artery, basal differentiation, and APC apoptosis (α_{13}, α_{23}, β_3, P_{hy}, r_{hy}, β_0, and η_1 removed) with threshold value $\tau = 4.05$ are illustrated in Fig. 5.

We observe from Fig. 5 that the posterior distributions best fit three different types of classic distributions: Uniform $U(\text{lower}, \text{upper})$, Normal $N(\mu, \sigma)$, and Weibull $W(A, B)$, and the corresponding distribution parameters are given in Table 4. Aiming to reduce the model further, we notice that none of the parameters have a heavy density near zero. Alternatively, we test two additional model reductions using different criteria.

First, parameters that exhibit Uniform posterior distributions are insensitive, implying that changes in the parameter value do not result in much better or much worse fits to the data. When parameters are insensitive, the usual procedure in sensitivity analysis is to fix them to a single value (Saltelli et al. 2008). Hence, in Sect. 4.4 we consider a reduced model with the APC proliferation rate with respect to the choroid oxygen, α_{11}, and the mass action rate, β_4, set to zero, as both parameters are best fit by Uniform distributions.

Second, as biological literature supports the assumptions that oxygen does not play a large role in promoting differentiation of APCs and IPAs or in promoting IPA proliferation, as we will discuss in Sect. 4.5, we consider a reduced model without the IPA proliferation rate with respect to choroid oxygen, α_{22}, and differentiation rate with respect to choroid oxygen, β_2.

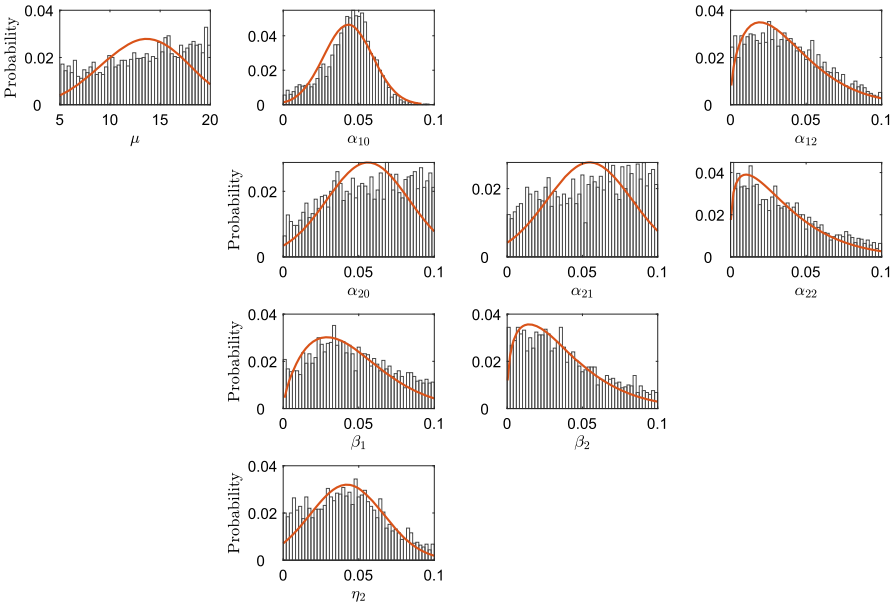

Fig. 6 ABC posterior distributions of 9 parameters to be estimated (Table 2) for the model (Sect. 4.4) without the hyaloid artery, basal differentiation, APC apoptosis, APC proliferation with respect to choroid oxygen, or mass action rate (α_{13}, α_{23}, β_3, P_{hy}, r_{hy}, β_0, η_1, α_{11} and β_4 removed) obtained from using Latin hypercube (LH) sampling with 500,000 LH points as prior distributions as described in Sect. 3. The parameter sets with error (23) less than threshold $\tau = 3.8$ are shown in the histograms. The solid red curves represent the best fitting probability distribution via minimizing the 1-Wasserstein metric (Table 4) (Color figure online)

4.4 Model Without Uniform Distributions (9 Parameters)

The posterior distributions obtained using the model with 9 parameters without the hyaloid artery, basal differentiation, APC apoptosis, APC proliferation with respect to choroid oxygen, and mass action rate (α_{13}, α_{23}, β_3, P_{hy}, r_{hy}, β_0, η_1, α_{11} and β_4 removed) with threshold value $\tau = 3.8$ are illustrated in Fig. 6.

We observe from Fig. 6 that the posterior distributions best fit two different types of classic distributions: Normal $N(\mu, \sigma)$ and Weibull $W(A, B)$, and the corresponding distribution parameters are given in Table 4. Aiming to reduce the model further, α_{12}, α_{21}, β_1 and β_2 are right-skewed best fit by Weibull distributions.

While the differentiation rate with respect to choroid oxygen, β_2, may be a realistic choice to set equal to zero (see reasoning below in Sect. 4.5), setting the APC and IPA proliferation rates with respect to PDGFA, α_{12} and α_{21}, to zero is unlikely to be physically-relevant since PDGFA has been experimentally identified as a promoter of proliferation (Mudhar et al. 1993; West et al. 2005; Fruttiger 2007; Tao and Zhang 2014). As PDGFA release is associated with the presence of retinal ganglion cells (RGCs), which mature over time, PDGFA is especially likely to have a nonzero influence on the proliferation rate of IPAs. If β_2 is set to zero, then β_1 could not also be set

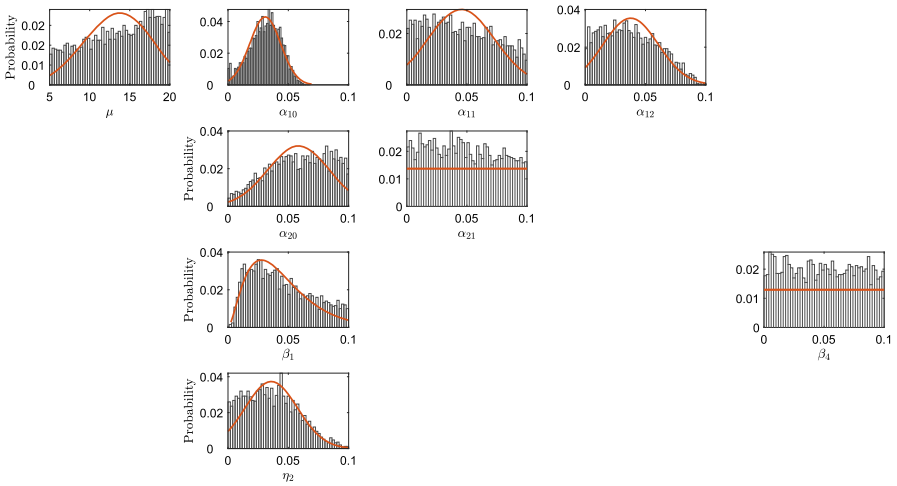

Fig. 7 ABC posterior distributions of 9 parameters to be estimated (Table 2) for the model (Sect. 4.5) without the hyaloid artery, basal differentiation, APC apoptosis, IPA proliferation with respect to choroid oxygen, or differentiation with respect to choroid oxygen ($\alpha_{13}, \alpha_{23}, \beta_3, P_{\text{hy}}, r_{\text{hy}}, \beta_0, \eta_1, \alpha_{22}$ and β_2 removed) obtained from using Latin hypercube (LH) sampling with 500,000 LH points as prior distributions as described in Sect. 3. The parameter sets with error (23) less than threshold $\tau = 3.7$ are shown in the histograms. The solid red curves represent the best fitting probability distribution via minimizing the 1-Wasserstein metric (Table 4) (Color figure online)

to zero since this would result in no astrocytes transitioning from APCs to IPAs in the model.

4.5 Model Without Choroid Oxygen for Differentiation and IPA Proliferation (9 Parameters)

While oxygen has been identified as playing a role in promoting proliferation of most cell types (Hubbi and Semenza 2015) and in promoting differentiation of astrocytes (Zhang et al. 1999; West et al. 2005; Duan et al. 2017), the levels of oxygen available during the later embryonic days of E15–E22/P0 may not be substantial enough to be necessary to include in a mathematical model.

Since oxygen supply from the choroid decreases and no longer diffuses to the retina by day E20 (Dollery et al. 1969; Braekevelt and Hollenberg 1970) and IPAs do not appear in significant numbers until after E19 (Chan-Ling et al. 2009, Fig. 2 G), there is not a large amount of oxygen physically available to promote IPA proliferation. Thus, it is reasonable that the IPA proliferation rate with respect to choroid oxygen, α_{22}, could be set to zero.

Duan et al. (2017) found that, since APC to IPA differentiation occurs far from retinal blood vessels, only low levels of oxygen are necessary, while higher levels of oxygen are required for IPAs to differentiate into mature astrocytes. It is reasonable that the differentiation rate with respect to choroid oxygen, β_2, could be set to zero if the low levels of oxygen are essentially negligible levels of oxygen.

Table 5 Marginal posterior distributions as approximated by (18) for various threshold values τ. m_1 = Full model (Sect. 4.1), m_2 = No Hyaloid model (Sect. 4.2), m_3 = No APC Apoptosis model (Sect. 4.3), m_4 = No Uniform model (Sect. 4.4), and m_5 = No Bio model (Sect. 4.5)

τ	$p(m_1 \mid \text{data})$	$p(m_2 \mid \text{data})$	$p(m_3 \mid \text{data})$	$p(m_4 \mid \text{data})$	$p(m_5 \mid \text{data})$
10^4	0.1982	0.1977	0.2005	0.2020	0.2017
35	0.2037	0.2009	0.1985	0.2001	0.1968
15	0.1910	0.2051	0.2107	0.1910	0.2022

The posterior distributions obtained using the model with 9 parameters without the hyaloid artery, basal differentiation, APC apoptosis, IPA proliferation with respect to choroid oxygen, or differentiation with respect to choroid oxygen (α_{13}, α_{23}, β_3, P_{hy}, r_{hy}, β_0, η_1, α_{22} and β_2 removed) with threshold value $\tau = 3.7$ are illustrated in Fig. 7.

We observe from Fig. 7 that the posterior distributions best fit four different types of classic distributions: Uniform $U(\text{lower, upper})$, Normal $N(\mu, \sigma)$, Gamma $\Gamma(a, b)$, and Weibull $W(A, B)$, and the corresponding distribution parameters are given in Table 4. Aiming to reduce the model further, we notice that none of the parameters have a heavy density near zero. Considering the parameters with Uniform posterior distributions, the IPA proliferation rate with respect to PDGFA, α_{21}, would not be a realistic choice to set equal to zero, based on the reasoning discussed in the previous Sect. 4.4. The other parameter with Uniform posterior distribution is the mass action rate β_4, which could potentially be set to zero as it was in the previous section.

4.6 Model Comparison

We use the ABC rejection model selection algorithm in the joint space-based approach (Sect. 3), sampling 150,000 parameter sets and report the marginal posterior distributions as approximated by (18) for various threshold values τ in Table 5. We notice that since all the values are approximately 0.2, this implies that the Bayes factor (19) for any two given models is approximately 1, and thus, there is weak evidence in favor of any model against the others.

However, we observed that when running individual ABC rejection for each model, the number of parameter sets in the prior distribution after the early stopping criteria was applied increased: 116,886 (Full model; Sect. 4.1); 309,848 (No Hyaloid model; Sect. 4.2); 468,397 (No APC Apoptosis model; Sect. 4.3); 473,708 (No Uniform model; Sect. 4.4); and 482,249 (No Bio model; Sect. 4.5). Additionally, the threshold value τ that corresponded with a 1% acceptance rate decreased among these models. Hence, this indicates that the reduced models may be better fits to the data, and a larger number of parameter sets using the model selection algorithm should be tested as we may not have sampled the space sufficiently.

From the numerical simulations illustrated in Fig. 2, we observe that the reduced models reflect the characteristic rim of APCs better and additional quantitative density data would be necessary to strengthen conclusions that could be made from model selection. In the next section, we discuss how biological literature supports the model reductions that arose from ABC rejection.

5 Discussion

In this work, we extended a mathematical model of astrocyte spreading and differentiation in the embryonic retina based on the previous model of Stepien and Secomb (2022). In our mathematical model, the mechanics of astrocyte spreading are represented by tension-driven growth, under the observation that traction forces are mainly generated at the leading edge in experimental astrocyte migration (De Pascalis et al. 2018). Various factors, such as oxygen supply and growth factor availability, promote astrocyte proliferation and differentiation from astrocyte precursor cells (APCs) to immature perinatal astrocytes (IPAs). In Stepien and Secomb (2022), a base mathematical model was developed to incorporate essential experimentally-observed mechanisms. Here, our aim was to include additional mechanisms and then compare between various nested reduced models using approximate Bayesian computation (ABC). Determining potential model reductions via right-skewed ABC posterior distributions gives insights into nonessential mechanisms that can be removed from the mathematical model equations.

In particular, based on the full mathematical model that we developed in Sect. 2, the following mechanisms of proliferation and differentiation do not appear to play a significant role: (1) oxygen supply from the hyaloid artery, (2) APC apoptosis, (3) choroid oxygen in promoting differentiation of APCs into IPAs, and (4) choroid oxygen in promoting IPA proliferation.

As the oxygen supply from the hyaloid artery does not effectively extend far from the optic nerve head (Shakib et al. 1968; Zhang et al. 1999), it is not surprising that our results indicate that it plays a negligible role. Indeed, this mechanism was not included in the previous mathematical model of Stepien and Secomb (2022). Our model reduction results here indicate that the choice to only include the choroid oxygen supply was appropriate.

Experimental work in Chan-Ling et al. (2009) demonstrated that while many IPAs underwent apoptosis, there was no evidence of APCs undergoing apoptosis. We included the effect of apoptosis in the growth functions for both the APCs and IPAs (3) for generality, however, our model reduction results here indicate that apoptosis of APCs is not a necessary model component.

Oxygen is readily available from the choroid vasculature at the beginning of the embryonic time period we focused on, yet the amount of oxygen that is able to diffuse all the way to the nerve fiber layer, where astrocytes are located, decreases over time as the retina thickens (Dollery et al. 1969; Braekevelt and Hollenberg 1970). As it has been experimentally observed that only low levels of oxygen are needed for APC to IPA differentiation (Duan et al. 2017), our model corroborates that the role of choroid oxygen in promoting differentiation is negligible. Additionally, due to the decrease of choroid oxygen supply to zero by day E20, there is not enough oxygen physically available to significantly promote IPA proliferation, and thus, our model reduction results here indicate that choroid oxygen promotion of IPA proliferation is not an essential mechanism.

These model selection results using ABC are very promising, as they verify experimental observations; however, future study should be done to continue analyzing the hypotheses. Although we varied both the parameter ranges in specifying the prior

distributions and the error function (23) used to calculate the difference between simulation output and experimental data to run multiple pre-tests of the ABC method, before running the final tests in Sect. 4, the choice of the prior distributions for the parameters and the error function can play a large role in the resulting posterior distributions of accepted parameter values, so one must proceed with caution (Robert et al. 2011; Sunnåker et al. 2013). There are also other ABC implementations such as a sequential Monte Carlo version of ABC called ABC-SMC (Toni et al. 2009; Drovandi and Pettitt 2011; Sisson et al. 2007) that are more efficient in obtaining approximate posterior distributions and performing model selection. However, as the experimental data set was small (Sect. 3.1), more detailed data would be necessary to do an expansive parameter estimation and comprehensive model comparison such as more replicates, quantified cell densities, and additional time points. The ABC rejection method is useful for providing preliminary information about reasonable parameter distributions and model choices even in cases of limited data.

Although astrocytes have long been thought to only passively support the central nervous system (CNS), recent discoveries have indicated their role and treatment potential in autism and neurological diseases such as traumatic brain injury, stroke, epilepsy, Alzheimer's disease, Parkinson's disease, Huntington's disease, and amyotrophic lateral sclerosis (ALS or Lou Gehrig's disease) (Caiazzo et al. 2015; Lange et al. 2012; Lepore et al. 2008; Proschel et al. 2014; Sloan and Barres 2014). As the retina is the only part of the CNS that can be noninvasively observed and measured, it is a convenient model system for the CNS, and obtaining information about the mechanisms of spreading and differentiation of retinal astrocytes during embryonic development is relevant to other parts of the CNS both during development and in later stages of life.

Supplementary Information

The details of the numerical method developed for solving the mathematical model equations and boundary and initial conditions as described in Sect. 2, parameter values used in the simulations in Fig. 2, and details of how the threshold value τ was chosen for the ABC rejection method are available in Online Resource 1.

Supplementary Information The online version contains supplementary material available at https://doi.org/10.1007/s11538-024-01354-5.

Acknowledgements The author acknowledges University of Florida Research Computing for providing computational resources and support that have contributed to the research results reported in this publication. The author additionally would like to thank the anonymous reviewers for their careful reading and many helpful suggestions.

Author Contributions Not applicable.

Funding The work was supported in part by National Science Foundation grant DMS-2151566.

Data Availability The author confirms that all data generated or analyzed during this study are included in this published article or can be reproduced from the computer code.

Code Availability The computer code used to generate the results for this article is available through GitHub at https://github.com/tstepien/astrocyte-migration-ABC [v1.0.0]. The code is platform independent and written in MATLAB, which requires a license. MATLAB data files produced by the code are available through OSF at https://osf.io/rm5qj/.

Declarations

Conflict of interest The author has no conflict of interest to declare.

Ethics Approval and Consent to Participate Not applicable.

Consent for Publication Not applicable.

References

Anand-Apte B, Hollyfield J (2010) Developmental anatomy of the retinal and choroidal vasculature. In: Dartt DA (ed) Encyclopedia of the eye. Academic Press, Boston, MA, pp 9–15. https://doi.org/10.1016/B978-0-12-374203-2.00169-X

Anderson HG, Takacs GP, Harris DC et al (2024) Global stability and parameter analysis reinforce therapeutic targets of PD-L1-PD-1 and MDSCs for glioblastoma. J Math Biol 88(1):10. https://doi.org/10.1007/s00285-023-02027-y

Aubert M, Chaplain MAJ, McDougall SR et al (2011) A continuum mathematical model of the developing murine retinal vasculature. Bull Math Biol 73(10):2430–2451. https://doi.org/10.1007/s11538-011-9631-y

Berson D (1965) The development of the choroid and sclera in the eye of the foetal rat with particular reference to their developmental interrelationship. Exp Eye Res 4(2):102–103, IN3–IN9. https://doi.org/10.1016/S0014-4835(65)80018-5

Braekevelt CR, Hollenberg MJ (1970) The development of the retina of the albino rat. Am J Anat 127(3):281–301. https://doi.org/10.1002/aja.1001270305

Browning AP, McCue SW, Simpson MJ (2017) A Bayesian computational approach to explore the optimal duration of a cell proliferation assay. Bull Math Biol 79(8):1888–1906. https://doi.org/10.1007/s11538-017-0311-4

Browning AP, Jin W, Plank MJ et al (2020) Identifying density-dependent interactions in collective cell behaviour. J R Soc Interface 17(165):20200143. https://doi.org/10.1098/rsif.2020.0143

Burkardt J (2021) latin_random: a MATLAB code which makes Latin random squares. https://people.sc.fsu.edu/~jburkardt/m_src/latin_random/latin_random.html, Retrieved 4 Jan 2024

Caiazzo M, Giannelli S, Valente P et al (2015) Direct conversion of fibroblasts into functional astrocytes by defined transcription factors. Stem Cell Rep 4(1):25–36. https://doi.org/10.1016/j.stemcr.2014.12.002

Carr MJ, Simpson MJ, Drovandi C (2021) Estimating parameters of a stochastic cell invasion model with fluorescent cell cycle labelling using approximate Bayesian computation. J R Soc Interface 18(182):20210362. https://doi.org/10.1098/rsif.2021.0362

Chan-Ling T, Chu Y, Baxter L et al (2009) In vivo characterization of astrocyte precursor cells (APCs) and astrocytes in developing rat retinae: differentiation, proliferation, and apoptosis. Glia 57(1):39–53. https://doi.org/10.1002/glia.20733

Cunha A Jr, Barton DAW, Ritto TG (2023) Uncertainty quantification in mechanistic epidemic models via cross-entropy approximate Bayesian computation. Nonlinear Dyn 111(10):9649–9679. https://doi.org/10.1007/s11071-023-08327-8

da Costa JMJ, Orlande HRB, da Silva WB (2018) Model selection and parameter estimation in tumor growth models using approximate Bayesian computation-ABC. Comput Appl Math 37(3):2795–2815. https://doi.org/10.1007/s40314-017-0479-0

De Pascalis C, Pérez-González C, Seetharaman S et al (2018) Intermediate filaments control collective migration by restricting traction forces and sustaining cell–cell contacts. J Cell Biol 217(9):3031–3044. https://doi.org/10.1083/jcb.201801162

Dollery CT, Bulpitt CJ, Kohner EM (1969) Oxygen supply to the retina from the retinal and choroidal circulations at normal and increased arterial oxygen tensions. Invest Ophthalmol 8(6):588–594
Drovandi CC, Pettitt AN (2011) Estimation of parameters for macroparasite population evolution using approximate Bayesian computation. Biometrics 67:225–233. https://doi.org/10.1111/j.1541-0420.2010.01410.x
Duan LJ, Pan SJ, Sato TN et al (2017) Retinal angiogenesis regulates astrocytic differentiation in neonatal mouse retinas by oxygen dependent mechanisms. Sci Rep 7(1):17608. https://doi.org/10.1038/s41598-017-17962-2
Dutta R, Chopard B, Lätt J et al (2018) Parameter estimation of platelets deposition: approximate Bayesian computation with high performance computing. Front Physiol. https://doi.org/10.3389/fphys.2018.01128
Francois O, Laval G (2011) Deviance information criteria for model selection in approximate Bayesian computation. Stat Appl Genet Mol Biol 10(1):33. https://doi.org/10.2202/1544-6115.1678
Fruttiger M (2007) Development of the retinal vasculature. Angiogenesis 10(2):77–88. https://doi.org/10.1007/s10456-007-9065-1
Fukushima M, Setoguchi T, Komiya S et al (2009) Retinal astrocyte differentiation mediated by leukemia inhibitory factor in cooperation with bone morphogenetic protein 2. Int J Devl Neurosci 27(7):685–690. https://doi.org/10.1016/j.ijdevneu.2009.07.006
Fung TH, Patel B, Wilmot EG et al (2022) Diabetic retinopathy for the non-ophthalmologist. Clin Med (Lond) 22(2):112–116. https://doi.org/10.7861/clinmed.2021-0792
Golub AS, Pittman RN (2012) Oxygen dependence of respiration in rat spinotrapezius muscle in situ. Am J Physiol Heart Circ Physiol 303:H47–H56. https://doi.org/10.1152/ajpheart.00131.2012
Goriely AR, Secomb TW, Tolbert LP (2002) Effect of the glial envelope on extracellular K(+) diffusion in olfactory glomeruli. J Neurophysiol 87(4):1712–1722. https://doi.org/10.1152/jn.00569.2001
Grelaud A, Marin JM, Robert CP et al (2009) ABC likelihood-free methods for model choice in Gibbs random fields. Bayesian Anal 4(2):317–335. https://doi.org/10.1214/09-BA412
Hellström A, Smith LE, Dammann O (2013) Retinopathy of prematurity. Lancet 382:1445–1457. https://doi.org/10.1016/S0140-6736(13)60178-6
Hubbi ME, Semenza GL (2015) Regulation of cell proliferation by hypoxia-inducible factors. Am J Physiol Cell Physiol 309(12):C775–C782. https://doi.org/10.1152/ajpcell.00279.2015
Johnston ST, Ross JV, Binder BJ et al (2016) Quantifying the effect of experimental design choices for in vitro scratch assays. J Theor Biol 400:19–31. https://doi.org/10.1016/j.jtbi.2016.04.012
Kass RE, Raftery AE (1995) Bayes factors. J Am Stat Assoc 90:773–795. https://doi.org/10.1080/01621459.1995.10476572
Kursawe J, Baker RE, Fletcher AG (2018) Approximate Bayesian computation reveals the importance of repeated measurements for parameterising cell-based models of growing tissues. J Theor Biol 443:66–81. https://doi.org/10.1016/j.jtbi.2018.01.020
Lange SC, Bak LK, Waagepetersen HS et al (2012) Primary cultures of astrocytes: their value in understanding astrocytes in health and disease. Neurochem Res 37(11):2569–2588. https://doi.org/10.1007/s11064-012-0868-0
Lepore AC, Rauck B, Dejea C et al (2008) Focal transplantation-based astrocyte replacement is neuroprotective in a model of motor neuron disease. Nat Neurosci 11(11):1294–1301. https://doi.org/10.1038/nn.2210
Liepe J, Kirk P, Filippi S et al (2014) A framework for parameter estimation and model selection from experimental data in systems biology using approximate Bayesian computation. Nat Protoc 9(2):439–456. https://doi.org/10.1038/nprot.2014.025
Marshall G (1986) A front tracking method for one-dimensional moving boundary problems. SIAM J Sci and Stat Comput 7(1):252–263. https://doi.org/10.1137/0907017
Martina Perez S, Sailem H, Baker RE (2022) Efficient Bayesian inference for mechanistic modelling with high-throughput data. PLOS Comput Biol 18(6):1–25. https://doi.org/10.1371/journal.pcbi.1010191
McDougall SR, Watson MG, Devlin AH et al (2012) A hybrid discrete-continuum mathematical model of pattern prediction in the developing retinal vasculature. Bull Math Biol 74(10):2272–2314. https://doi.org/10.1007/s11538-012-9754-9
Mi H, Barres BA (1999) Purification and characterization of astrocyte precursor cells in the developing rat optic nerve. J Neurosci 19(3):1049–1061
Mi H, Haeberle H, Barres BA (2001) Induction of astrocyte differentiation by endothelial cells. J Neurosci 21(5):1538–1547. https://doi.org/10.1523/JNEUROSCI.21-05-01538.2001

Mudhar HS, Pollock RA, Wang C et al (1993) PDGF and its receptors in the developing rodent retina and optic nerve. Development 118(2):539–552
Popel AS (1989) Theory of oxygen transport to tissue. Crit Rev Biomed Eng 17(3):257–321
Prangle D (2016) Lazy ABC. Stat Comp 26:171–185. https://doi.org/10.1007/s11222-014-9544-3
Proschel C, Stripay JL, Shih CH et al (2014) Delayed transplantation of precursor cell-derived astrocytes provides multiple benefits in a rat model of parkinsons. EMBO Mol Med 6(4):504–518. https://doi.org/10.1002/emmm.201302878
Robert CP, Cornuet JM, Marin JM et al (2011) Lack of confidence in approximate Bayesian computation model choice. Proc Natl Acad Sci USA 108(37):15112–15117. https://doi.org/10.1073/pnas.1102900108
Saint-Geniez M, D'Amore PA (2004) Development and pathology of the hyaloid, choroidal and retinal vasculature. Int J Dev Biol 48(8–9):1045–1058. https://doi.org/10.1387/ijdb.041895ms
Saltelli A, Ratto M, Andres T et al (2008) Global sensitivity analysis: the primer. Wiley, Hoboken, NJ
Secomb TW (2015) Computational methods for modeling retinal hemodynamics and oxygen transport. In: Nithiarasu P, Budyn E (eds) 4th international conference on computational and mathematical biomedical engineering—CMBE2015, pp 612–615
Shakib M, De Oliveira LF, Henkind P (1968) Development of retinal vessels. II. Earliest stages of vessel formation. Invest Ophthalmol 7(6):689–700
Sisson SA, Fan Y, Tanaka MM (2007) Sequential Monte Carlo without likelihoods. Proc Natl Acad Sci USA 104:1760–1765. https://doi.org/10.1073/pnas.0607208104
Sisson SA, Fan Y, Beaumont MA (eds) (2019) Handbook of approximate Bayesian computation. CRC Press, Boca Raton, FL
Sloan SA, Barres BA (2014) Mechanisms of astrocyte development and their contributions to neurodevelopmental disorders. Curr Opin Neurobiol 27:75–81. https://doi.org/10.1016/j.conb.2014.03.005
Stepien TL, Secomb TW (2022) Spreading mechanics and differentiation of astrocytes during retinal development. J Theor Biol 549:111208. https://doi.org/10.1016/j.jtbi.2022.111208
Stepien TL, Lynch HE, Yancey SX et al (2019) Using a continuum model to decipher the mechanics of embryonic tissue spreading from time-lapse image sequences: an approximate Bayesian computation approach. PLOS One 14(6):e0218021. https://doi.org/10.1371/journal.pone.0218021
Stone J, Itin A, Alon T et al (1995) Development of retinal vasculature is mediated by hypoxia-induced vascular endothelial growth factor (VEGF) expression by neuroglia. J Neurosci 15(7):4738–4747. https://doi.org/10.1523/JNEUROSCI.15-07-04738.1995
Sunnåker M, Busetto AG, Numminen E et al (2013) Approximate Bayesian computation. PLOS Comput Biol 9(1):e1002803. https://doi.org/10.1371/journal.pcbi.1002803
Syková E, Nicholson C (2008) Diffusion in brain extracellular space. Physiol Rev 88(4):1277–1340. https://doi.org/10.1152/physrev.00027.2007
Tanaka MM, Francis AR, Luciani F et al (2006) Using approximate Bayesian computation to estimate tuberculosis transmission parameters from genotype data. Genetics 173(3):1511–1520. https://doi.org/10.1534/genetics.106.055574
Tao C, Zhang X (2014) Development of astrocytes in the vertebrate eye. Dev Dyn 243(12):1501–1510. https://doi.org/10.1002/dvdy.24190
Toni T, Stumpf MPH (2009) Simulation-based model selection for dynamical systems in systems and population biology. Bioinformatics 26(1):104–110. https://doi.org/10.1093/bioinformatics/btp619
Toni T, Welch D, Strelkowa N et al (2009) Approximate Bayesian computation scheme for parameter inference and model selection in dynamical systems. J R Soc Interface 6:187–202. https://doi.org/10.1098/rsif.2008.0172
Vo BN, Drovandi CC, Pettitt AN et al (2015) Quantifying uncertainty in parameter estimates for stochastic models of collective cell spreading using approximate Bayesian computation. Math Biosci 263:133–142. https://doi.org/10.1016/j.mbs.2015.02.010
Wang X, Jenner AL, Salomone R et al (2024) Calibration of agent based models for monophasic and biphasic tumour growth using approximate Bayesian computation. J Math Biol 88(3):28. https://doi.org/10.1007/s00285-024-02045-4
Warne DJ, Baker RE, Simpson MJ (2019) Using experimental data and information criteria to guide model selection for reaction-diffusion problems in mathematical biology. Bull Math Biol 81(6):1760–1804. https://doi.org/10.1007/s11538-019-00589-x

Watson MG, McDougall SR, Chaplain MAJ et al (2012) Dynamics of angiogenesis during murine retinal development: a coupled in vivo and in silico study. J R Soc Interface 9:2351–2364. https://doi.org/10.1098/rsif.2012.0067

West H, Richardson WD, Fruttiger M (2005) Stabilization of the retinal vascular network by reciprocal feedback between blood vessels and astrocytes. Development 132(8):1855–1862. https://doi.org/10.1242/dev.01732

Xiao Y, Thomas L, Chaplain MAJ (2021) Calibrating models of cancer invasion: parameter estimation using approximate Bayesian computation and gradient matching. R Soc Open Sci 8(6):202237. https://doi.org/10.1098/rsos.202237

Yu DY, Cringle SJ, Yu PK et al (2007) Intraretinal oxygen distribution and consumption during retinal artery occlusion and graded hyperoxic ventilation in the rat. Invest Ophthalmol Vis Sci 48(5):2290–2296. https://doi.org/10.1167/iovs.06-1197

Zhang Y, Porat RM, Alon T et al (1999) Tissue oxygen levels control astrocyte movement and differentiation in developing retina. Brain Res Dev Brain Res 118(1–2):135–145. https://doi.org/10.1016/S0165-3806(99)00140-6